

Spiers Memorial Lecture: activating metal sites for biological electron transfer

Edward I. Solomon *^{ab} and Anex Jose ^a

Received 6th January 2022, Accepted 17th January 2022

DOI: 10.1039/d2fd00001f

Metal sites in biology often exhibit unique spectroscopic features that reflect novel geometric and electronic structures imposed by the protein that are key to reactivity. The blue copper active site involved in long range, rapid biological electron transfer is a classic example. This review presents an overview of both traditional and synchrotron based spectroscopic methods and their coupling to electronic structure calculations to understand the unique features of the blue copper active site, their contributions to function and the role of the protein in determining the geometric and electronic structure of the active site (called the "entatic state"). The relation of this active site to other biological electron transfer sites is further developed. In particular, ultrafast XFEL spectroscopy is used to evaluate the methionine–S–Fe bond in cytochrome *c*, and its entatic control by the protein in determining function (electron transfer vs. apoptosis).

In Bioinorganic Chemistry, we mostly focus on a small region of the large biomolecule that is the metal and its ligands, as this is the active site for catalysis (Fig. 1).¹ The wide range of spectroscopic methods of physical-inorganic chemistry that are used to probe these active sites are summarized below.²

1. Spectroscopy and electronic structure calculations

The left side of Fig. 2 shows the complete electronic structure diagram for square planar D_{4h} -[CuCl₄]²⁻ (d⁹) that will be a useful reference in this presentation.⁴ All energy levels are occupied up to the highest energy half-occupied $d_{x^2-y^2}$ orbital that is the GS. On the right in Fig. 2 are the main spectroscopic methods of physical inorganic chemistry ordered by increasing energy. At low resolution, the GS is studied by magnetic susceptibility and, for ⁵⁷Fe, Mössbauer spectroscopy. These mostly give the redox and spin states of the metal site. At higher resolution, the GS is studied by electron paramagnetic resonance (EPR) spectroscopy, which

^aDepartment of Chemistry, Stanford University, Stanford, CA 94305, USA. E-mail: solomone@stanford.edu

^bStanford Synchrotron Radiation Lightsource, SLAC National Accelerator Laboratory, Stanford University, Menlo Park, CA 94025, USA

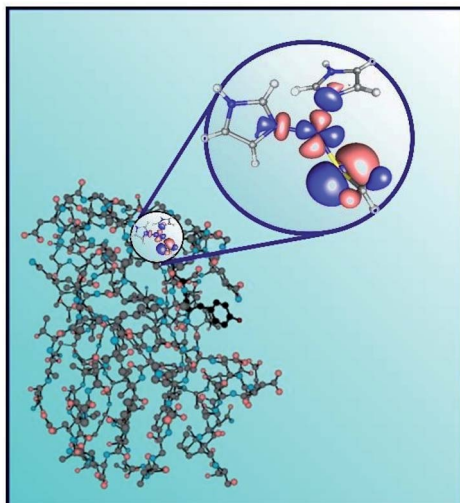


Fig. 1 The protein as a whole with its active site and ground state (GS) wave function in the expanded scale. Reprinted with permission from ref. 3. Copyright (2006) American Chemical Society.

gives the g_i values that define the nature of the half-occupied orbital (*i.e.* whether the electron is in the $d_{x^2-y^2}$ or d_{z^2} orbital) and the hyperfine couplings of the electron spin with the metal and the ligand nuclear spins that define its delocalization. This delocalization is probed at a still higher resolution using double

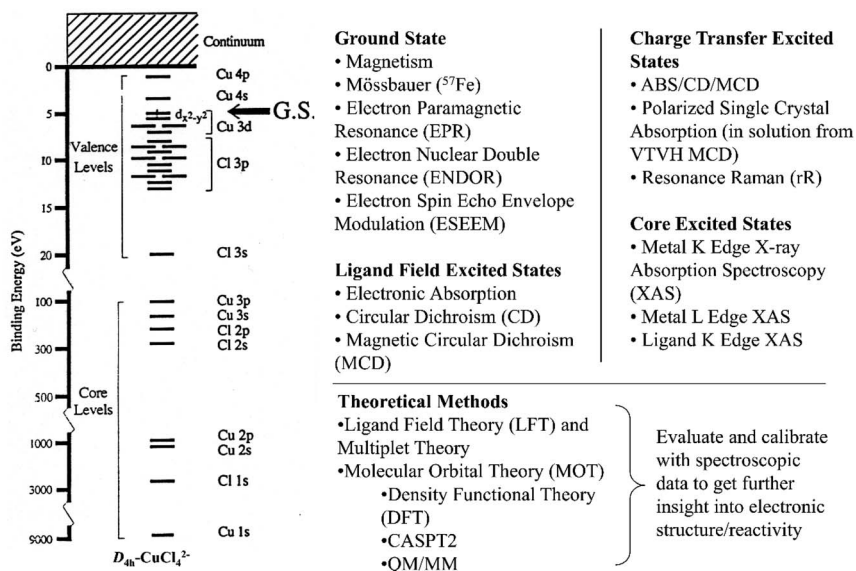


Fig. 2 Electronic structure diagram of D_{4h} - $[\text{CuCl}_4]^{2-}$ (left) and spectroscopic and electronic structure methods used in Bioinorganic Chemistry (right). Reprinted with permission from ref. 3. Copyright (2006) American Chemical Society.

resonance and pulsed EPR methods. These GS studies are generally done in a magnetic field using a microwave source at an energy in the order of 1 cm^{-1} .

Going up into the near-infrared (near-IR)/visible (Vis) energy range, electrons from the filled d orbitals in Fig. 2 (left) are excited into the half-occupied $d_{x^2-y^2}$ orbital, producing ligand field (LF) transitions. These $d \rightarrow d$ transitions are parity forbidden and, hence, weak in absorption, but can be studied by circular dichroism (CD) (in an optically active site as is generally the case in metalloproteins) and in magnetic CD (MCD) in a longitudinal magnetic field at low temperatures, as their different selection rules enhance the LF transition intensities. It is important to note that the energy splittings of the LF states are sensitive to the ligand environment of the metal active site and, thus, probe geometry and bonding.

At higher energies [Vis/ultra-violet (UV)], the photon can excite electrons from the filled ligand-based valence molecular orbitals into the hole in the $d_{x^2-y^2}$ orbital, shown in the left hand side of Fig. 2. These are the ligand to metal charge transfer (LMCT) transitions and, since they involve transfer of the electron from a formally ligand-centered molecular orbital to a formally metal-centered molecular orbital, they are electric dipole allowed, hence intense in the absorption spectrum (and relatively weak in CD and MCD) and polarized along the L-M bond. These highly intense transitions enable tuning a laser into the absorption band to resonance enhance the Raman vibrational modes of the active site specific to the CT state in resonance. These CT transitions directly probe the σ - and π -bonding interactions of the specific ligand with the metal center.

Proceeding to still higher energies, now using a synchrotron for intense, polarized, continuous X-ray photons, electrons are excited from filled metal and ligand core levels into the half-occupied d orbital. For D_{4h} -[CuCl₄]²⁻, these are the Cu K-edge at 8979 eV, the Cu L-edge at 930 eV and the Cl K-edge at 2820 eV. As will be presented below, these directly define the GS wave function of a metal active site.

These methods define the electronic structure experimentally. It is important then to correlate these results to electronic structure calculations. These are generally of two types. Ligand field theory (LFT) focuses on the ground and low-lying LF excited states. It is quite powerful if the metal site is not very covalent. For more covalent sites and to correlate to the complete energy level diagram in Fig. 2, molecular orbital theory is required, and this mostly means density functional theory (DFT). However, there are a range of different functionals and hybrids and these calculations can give significantly different electronic structure descriptions. Thus, it is important to correlate calculations to experiments and, when supported by spectroscopy, these can provide detailed insight into frontier molecular orbitals (FMO) and reaction coordinates in catalysis.

There are two general goals of spectroscopy in Bioinorganic Chemistry: (1) to determine the active site geometric and electronic structure and understand how structure leads to function and (2) to define the reaction mechanism on a molecular level. The latter involves using the different spectroscopic methods of Fig. 2 to define the reaction intermediates and calculations supported by these spectroscopic data to evaluate the reaction coordinates. These general goals have led to important spectroscopic goals. One has been the development of new spectroscopic methods to address important problems in Bioinorganic Chemistry that were not accessible through existing methods. The second has been to

understand the unique spectroscopic features observed for many major classes of active sites in biology (relative to small molecule inorganic complexes of the same metal ion). These reflect novel geometric and electronic structures that are imposed on the metal site by the protein (as in Fig. 1) that activate the metal site for function. This presentation will emphasize these goals, where a range of spectroscopies (including new spectroscopic methods) coupled with electronic structure calculations are used to understand the unique spectral features of the blue Cu proteins that function in rapid, long range electron transfer (ET) in biology. Since the focus of this presentation is on unique spectroscopic features, we first summarize the “normal” structural and spectral features of Cu(II) complexes using D_{4h} -[CuCl₄]²⁻ as a reference.

2. Geometric and electronic structure of “normal” Cu(II) complexes

From Fig. 3A, placing a Cu(II) ion in an octahedral field splits the five d-orbitals into an e_g set above the t_{2g} set by $10 D_q$ (Fig. 3B left). Cu(II) has 9 d-electrons, resulting in an electron hole in the e_g set, giving a 2E_g ground state. This is orbitally degenerate and, thus, undergoes a Jahn–Teller distortion of the site that splits the orbital degeneracy and lowers the energy of the system. Cu(II) complexes generally show a tetragonal elongation along the z-axis and contraction in the

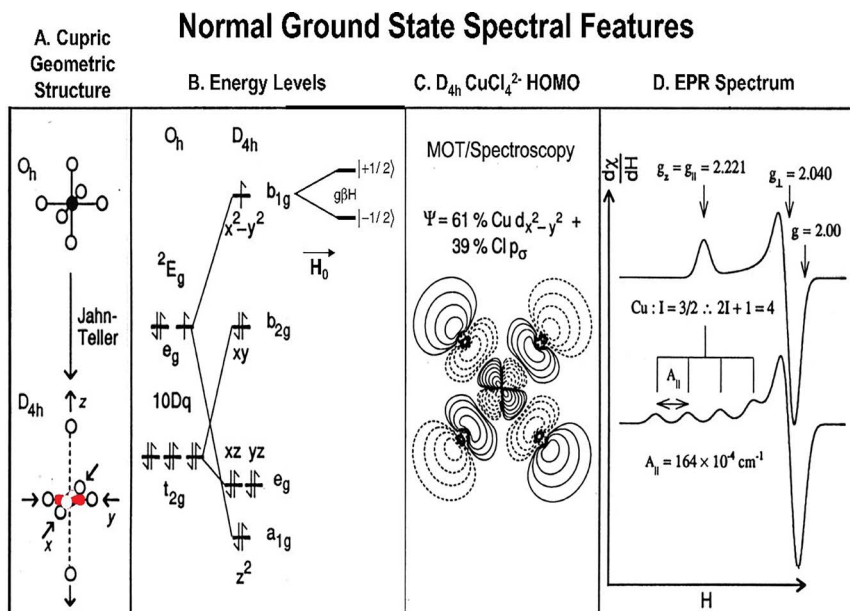


Fig. 3 Normal Cu(II) complexes. (A) Cupric geometric structure in O_h symmetry and upon Jahn–Teller distortion to D_{4h} ; the highest energy half-occupied $d_{x^2-y^2}$ orbital is highlighted in red, (B) Energy levels of Cu(II) d-orbitals in O_h and D_{4h} , and the Zeeman splitting of the GS in a magnetic field (H_0). (C) D_{4h} -[CuCl₄]²⁻ HOMO (from methods in Fig. 2) and (D) EPR spectrum without (top) and with (bottom) metal hyperfine coupling. Reprinted with permission from ref. 3. Copyright (2006) American Chemical Society.

bonding also controls the intensity of the CT transition (see inset in Fig. 4C), which is proportional to the overlap of the donor and acceptor orbitals involved in the LMCT transition. From Fig. 4C the $p\sigma$ has a significant overlap with the $d_{x^2-y^2}$ orbital and produces an intense CT transition at higher energy than the π CT (which has no overlap with $d_{x^2-y^2}$ but gains some intensity due to their configuration interaction).⁸ Thus, the Vis/UV absorption spectrum of D_{4h} -[CuCl₄]²⁻ shown in Fig. 4B (blue) has low energy weak π and high energy intense σ CT transitions. The EPR spectrum, shown in the bottom of Fig. 3D, and the absorption spectrum in Fig. 4B are characteristic of “normal” tetragonal Cu(II) complexes and serve as reference spectra for the unique spectral features of the blue Cu active sites and their relation to its ET function.

3. Electron transfer sites in Bioinorganic Chemistry

There are three classes of metal sites in biology that function in ET (Fig. 5). For copper proteins, there is the blue Cu site that is mononuclear with thiolate and thioether ligands, and Cu_A that is binuclear, also having thiolate (bridging) and thioether ligation. In iron–sulfur chemistry, there are the rubredoxins, ferredoxins and HiPIP (high potential iron protein) that have different nuclearities but all with tetrahedral sulfur ligand fields that are weak and function as high spin sites in both redox states. In heme chemistry, there are the cytochromes (cyt), all having strong equatorial porphyrin ligation and two axial ligands: cyt *c* has thioether and histidine as axial ligands. The cytochromes are low spin in both redox states.

There are quite a variety of structures and they cover almost a 2 V potential range, but there are two common features among all the sites in Fig. 5 enabling their efficient ET: (1) there is minimal geometry change with redox (*i.e.* a low reorganization energy (λ) in Marcus theory of ET)⁹ and (2) there is efficient electronic coupling between the electron donor and acceptor (H_{DA}), often over long distances through the protein. This presentation mostly focuses on how the

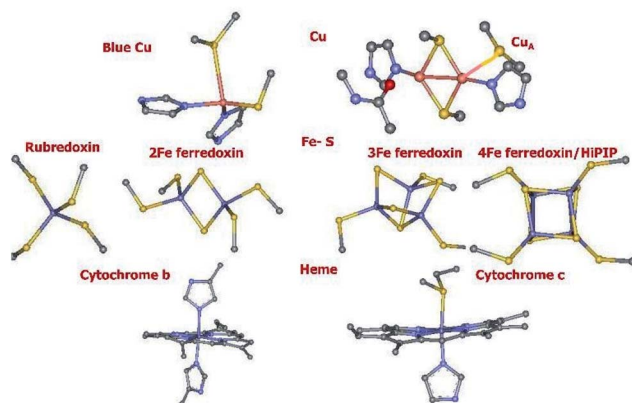


Fig. 5 Electron transfer sites in Bioinorganic Chemistry. Reprinted with permission from ref. 3. Copyright (2006) American Chemical Society.

unique spectral features of the blue Cu site reflect a geometric and electronic structure imposed by the protein that enables this ET function. These concepts are then extended to cyt *c* in the later part of this presentation.

4. The unique geometric and electronic structure of the blue copper active site

The first crystal structure of a blue Cu protein was that of plastocyanin, solved by Hans Freeman in 1978.¹⁰ As shown in Fig. 6A the Cu(II) site had a tetrahedral structure, not the tetragonal structure generally observed for normal Cu(II) complexes. This led to the idea that the protein must oppose the Jahn–Teller distortion of the oxidized site, thus activating it for rapid ET. This concept of the protein constraining the ligand environment of a metal site activating it for function is known as the “entatic state” in Bioinorganic Chemistry.^{11,12} The entatic nature of the blue Cu site will be elucidated later in this presentation. As mentioned above, the blue Cu site has two special ligands: a short cysteine (Cys) thiolate S–Cu(II) bond at 2.1 Å and a long methionine (Met) thioether S–Cu(II) bond at 2.9 Å. The remaining ligands are His N’s with fairly normal bond lengths.

Associated with the unique tetrahedral structure and Cys/Met ligation are the unique spectral features of the blue Cu proteins. Instead of weak LF transitions with $\epsilon \sim 40 \text{ M}^{-1} \text{ cm}^{-1}$ in the $16\,000 \text{ cm}^{-1}$ region, the blue Cu site has an intense absorption band ($\epsilon \sim 5000 \text{ M}^{-1} \text{ cm}^{-1}$) in this region (in Fig. 6B) and the magnitude of the parallel hyperfine splitting of the blue Cu site in Fig. 6C is reduced by more than a factor of two relative to that of normal Cu(II). It will now be elucidated that these unique spectral features reflect a novel GS wave function that is the redox active molecular orbital (RAMO) key to its biological function of long range rapid ET.

From Fig. 6C, the EPR spectrum of the blue Cu site in plastocyanin has $g_{\parallel} > g_{\perp} > 2.00$. From the LF spectroscopy in section 2, this requires that the half-occupied

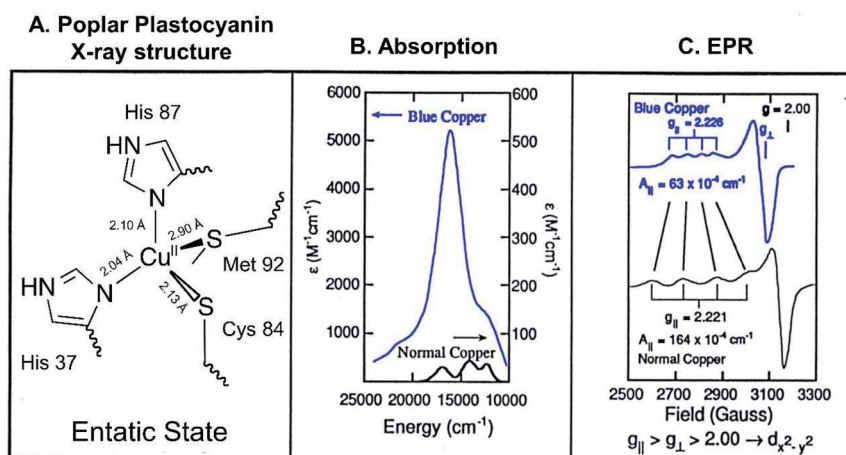


Fig. 6 Oxidized blue Cu site: (A) schematic of the X-ray structure of the blue Cu site in plastocyanin, (B) absorption and (C) EPR spectra of normal Cu(II) (black) and blue Cu (blue) sites. Reprinted with permission from ref. 3. Copyright (2006) American Chemical Society.

orbital is $d_{x^2-y^2}$ and this had to be correlated with the distorted tetrahedral geometric structure of the blue Cu site in Fig. 6A. This was accomplished by single crystal EPR spectroscopic studies of plastocyanin.¹³

Plastocyanin crystallizes in an orthorhombic space group with four symmetry related molecules in the unit cell. An expanded view of the active sites of these proteins is shown in Fig. 7A. Rotating the crystal around the a -axis with the field along different orientations in the b/c -plane produced the single crystal EPR spectra shown in the left hand side of Fig. 7B. It can be seen that the g_{\parallel} spectrum with the four observable hyperfine lines is present when the field is along the c -axis, while rotation by $\sim 90^\circ$ leads to a g_{\perp} EPR signal (Fig. 7B left bottom). Thus, g_{\parallel} is approximately along the c -axis of the unit cell which, from the expanded view in Fig. 7A, is the approximate orientation of the long Met thioether S-Cu bond. Three single crystal rotations were performed and simulated with the four molecules in the unit cell (Fig. 7B right), which locked in the g_{\parallel} at an angle of just 5° off the long (2.9 Å) Cu(II)-S_{Met} bond. Thus, the $d_{x^2-y^2}$ orbital, which is perpendicular to this direction, is in the plane of the strong Cu(II)-S_{Cys} and two Cu(II)-N_{His} bonds. This changed how the active site is visualized relative to the crystallography (Fig. 6A) and the focus is now on this $x^2 - y^2$ plane.

We now consider one of the unique spectral features of the blue Cu active site, the origin of the small metal parallel hyperfine splitting (A_{\parallel} in the top panel of Fig. 6C). As presented in Fig. 8, there are three contributions to the hyperfine coupling of the nuclear spin I of the Cu to the electron in the Cu $d_{x^2-y^2}$ orbital. These are: (1) the Fermi contact interaction of the electron spin with the nuclear spin at the nucleus, which is indirect and occurs through the spin polarization of core s-electrons; (2) the spin dipolar coupling of the electron spin averaged over the $d_{x^2-y^2}$ orbital with the nuclear spin on the Cu and (3) the orbital dipolar coupling of the electron with the nuclear spin that has the same origin as the g_i

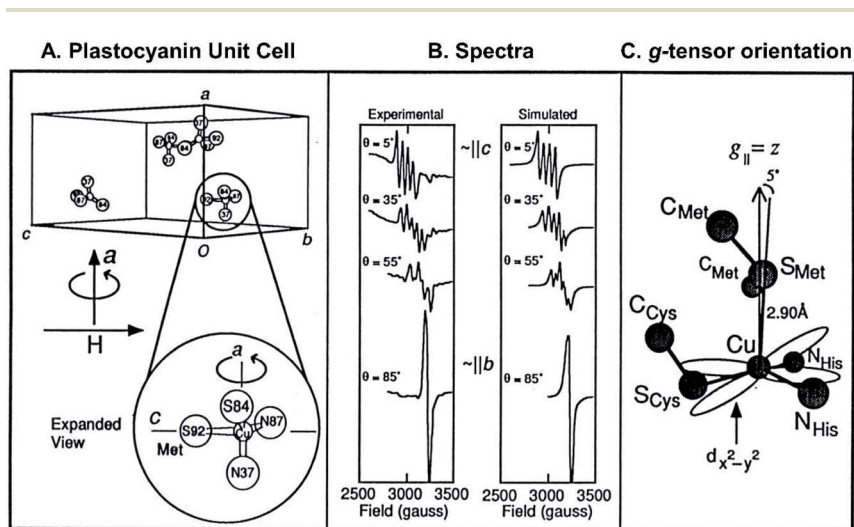


Fig. 7 Orientation of the $d_{x^2-y^2}$ orbital in plastocyanin from single crystal EPR spectroscopy. (A) Plastocyanin unit cell, (B) experimental (left) and simulated (right) single crystal EPR spectra, and (C) resultant g -tensor orientation. Reprinted with permission from ref. 3. Copyright (2006) American Chemical Society.

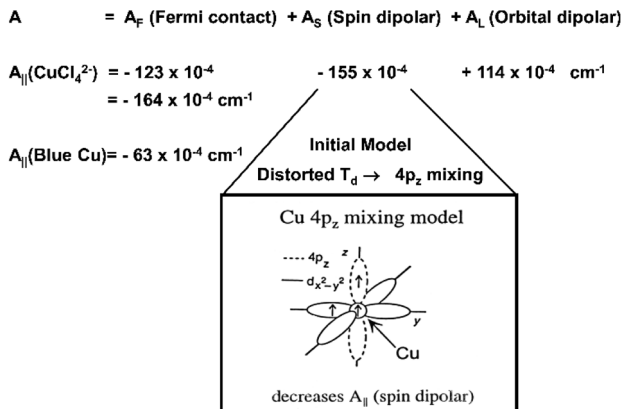


Fig. 8 The three contributions to the metal A_{\parallel} in the Cu(II) EPR spectrum and the initial model for the origin of the small $|A_{\parallel}|$ of the blue Cu site (inset). Reprinted with permission from ref. 3. Copyright (2006) American Chemical Society.

values deviating from 2.00 (*vide infra*) and can be estimated from these. As shown in Fig. 8, all three contributions are comparable in magnitude but have different signs and sum to the large negative A_{\parallel} of $-164 \times 10^{-4} \text{ cm}^{-1}$ observed for $D_{4h}\text{-}[\text{CuCl}_4]^{2-}$ in Fig. 3D. For the blue Cu site in plastocyanin, the magnitude of A_{\parallel} is greatly reduced to $-63 \times 10^{-4} \text{ cm}^{-1}$. Initially, this decreased magnitude of A_{\parallel} was assumed to derive from the distorted tetrahedral structure of the blue Cu site in Fig. 6A.¹⁴ This was reasonably thought to mix Cu $4p_z$ character into the $d_{x^2-y^2}$ orbital (dashed orbital in the inset of Fig. 8). Electron spin in this p_z orbital has the opposite sign for spin dipolar coupling with the nuclear spin on the Cu and $\sim 12\%$ $4p_z$ mixing would reduce the magnitude of A_{\parallel} to the experimental value for plastocyanin.

While this possibility was reasonable, it was important to evaluate it experimentally. This was accomplished by going up by 10^{10} in photon energy, from the 10^{-4} cm^{-1} region of hyperfine coupling to the $\sim 9000 \text{ eV}$ region of X-ray absorption spectroscopy at the Cu K-edge.¹⁵

As shown in Fig. 9A the Cu K-pre-edge $1s \rightarrow 3d$ transition occurs at 8979 eV. A pure $1s \rightarrow 3d$ transition is electric dipole forbidden and, thus, is very weak. However, the distorted T_d geometry of the blue Cu site enables $4p$ mixing into this RAMO and the $1s \rightarrow 4p$ transition is electric dipole allowed, so even a low percent mixing (α^2 in Fig. 9A) would give rise to dominant pre-edge intensity. As shown in Fig. 9B (arrow), the pre-edge intensity of the blue Cu XAS spectrum at 8979 eV is indeed much higher than that of $D_{4h}\text{-}[\text{CuCl}_4]^{2-}$, where $4p$ mixing is forbidden by group theory. The important experiment here was to determine the nature of the $4p$ mixing in plastocyanin. This was accomplished by the analysis of its polarized single crystal XAS data. The single crystal EPR studies in Fig. 7 showed that the electronic z -axis was approximately along the Cu– S_{Met} bond, so the polarized single crystal spectra obtained with the E vector of the synchrotron oriented along this bond would reveal the Cu $4p_z$ character. From the dashed $E||z$ spectrum in Fig. 9C, there is no pre-edge intensity, thus no Cu $4p_z$ mixing. Alternatively, when the E of the synchrotron is oriented in the (x,y) plane (the solid spectrum in

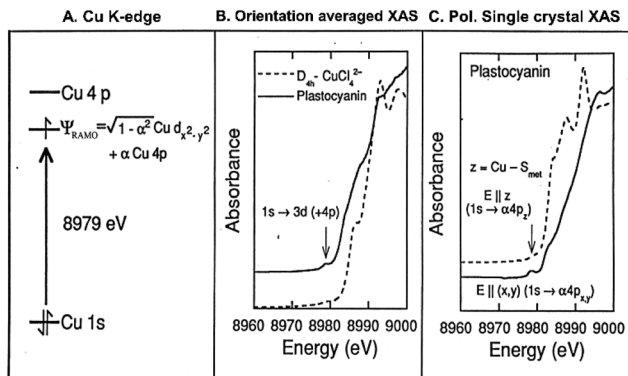


Fig. 9 X-ray absorption spectroscopy to evaluate the Cu 4p mixing into the $3d_{x^2-y^2}$ orbital in plastocyanin. (A) Cu K-pre-edge $1s \rightarrow 3d$ transition at 8979 eV, (B) orientation averaged XAS spectra of $D_{4h}^-[\text{CuCl}_4]^{2-}$ and plastocyanin and (C) Polarized single crystal XAS spectrum of plastocyanin with $E \parallel z$ and $E \parallel (x,y)$ (z -axis defined by the single crystal EPR in Fig. 7). Reprinted with permission from ref. 16. Copyright (2004) American Chemical Society.

Fig. 9C), dominant pre-edge intensity is observed. This Cu $4p_{x,y}$ mixing in plastocyanin demonstrated by these polarized XAS data would increase, not decrease the magnitude of the parallel hyperfine splitting. This eliminated the generally accepted explanation for the small A_{\parallel} of blue Cu sites and focused our attention on the alternative possibility for the small A_{\parallel} of blue Cu sites: a highly covalent GS which shifts the electron spin onto the ligand(s) and reduces its interaction with the nuclear spin on the Cu.

This possibility of a highly covalent blue Cu active site was initially addressed through a quantitative consideration of its g_i values.¹⁷ The table at the top of Fig. 10, left column, gives the experimental g_i values of plastocyanin. Moving from left to right in this table, for an unpaired electron in a pure $d_{x^2-y^2}$ orbital, thus having only spin angular momentum, the g_i values would be isotropic and equal to the spin only value of 2.0023. This is similar to what is observed in organic radicals where spin-orbit coupling (SOC) is small. However, transition metal sites have large values of their SOC parameter ($\lambda[\text{Cu}(\text{II})] = -830 \text{ cm}^{-1}$) and this mixes excited LF states into the GS, giving them an orbital angular momentum contribution to their g_i values. A complete LFT calculation of the blue Cu site in plastocyanin including SOC gives the g_i values in the third column of the table in Fig. 10, with $g_{\parallel} > g_{\perp} > 2.00$. However, these deviate too much from the experimental values in the first column. Thus, there is too much orbital angular momentum mixed into the GS. This is due to the nature of LFT that treats the orbitals as having pure metal d character. Covalency delocalizes the electron onto the ligand(s) and this decreases the orbital angular momentum in the GS. The fourth column in the table uses one of the earliest DFT methods (SCF- $X\alpha$ scattered wave) with SOC included to calculate the effects of covalency on the GS g_i values. Comparison to the third column demonstrates that covalency does indeed decrease the deviation from 2.00 relative to LFT, however comparison to the first column shows that these are decreased by too much, indicating that this “state of the art” calculation at the time (1985) overestimated the covalency of the blue Cu

	experimental Q-band EPR	$(x^2-y^2)^1$ spin only	L.F.T d orbitals + λ L·S	SCF-X α -SW LF + CT levels λ_{Cu} L·S + λ_L L·S Norman Radii	Adjusted Radii
g_x	2.047	2.00	2.125	2.046	2.059
g_y	2.059	2.00	2.196	2.067	2.076
g_z	2.226	2.00	2.479	2.159	2.226

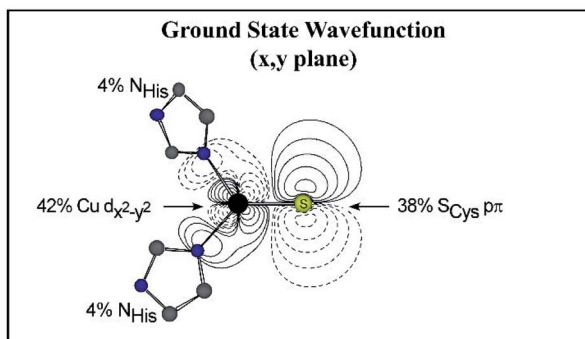


Fig. 10 Evaluation of the GS wave function of the blue Cu site in plastocyanin. The top table gives the g_i values observed experimentally (from Q-band EPR) and the corresponding values predicted by various electronic structure methods. The panel below shows the experimentally adjusted GS wave function in the (x,y) plane with % character on Cu and S_{Cys} and two N_{His} . Reprinted with permission from ref. 3. Copyright (2006) American Chemical Society.

site. Thus, parameters in this DFT calculation were adjusted to calculate a GS wave function that agrees with the experimental g_i values. This is shown below the table [in the (x,y) plane]. This was a major insight into the electronic structure of the blue Cu sites, as it showed a highly covalent GS which has 42% $d_{x^2-y^2}$ character, and this character is anisotropically delocalized into the thiolate ligand having 38% character and this delocalization involved the S_{Cys} π , not σ -orbital, of the thiolate.

While this experimentally adjusted DFT calculation was performed >35 years ago using a relatively simple code, modern DFT calculations give parallel results. From the model on the top half of the left hand side of Fig. 11 and the first two rows in the table on the right, both a pure functional (BP86) and a hybrid functional (B3LYP) containing 20% Hartree-Fock exchange gave equivalent GS wavefunctions, a $d_{x^2-y^2}$ orbital highly delocalized into the S $p\pi$ -orbital of the Cys sulfur ligand, but again too covalent with 30% Cu and 60% S_{Cys} compared to experiment (blue row, *vide infra*) with $\sim 40\%$ character on each.

However, the calculations using the model on the top left of Fig. 11 only included the first coordination sphere of the active site. Inclusion of the extended protein environment (modelled by QM/MM or using a large QM region, combined with a hybrid DFT method) now gives reasonable agreement with experiment, with $\sim 43\%$ of the wave function on the Cu and the S_{Cys} .^{3,18-20} Thus, the environment decreases the covalent delocalization onto the thiolate, and this reflects the combined effects of an H-bond of the backbone to the thiolate and nearby carbonyl dipoles. This change in the covalency of the Cu- S_{Cys} bond provides

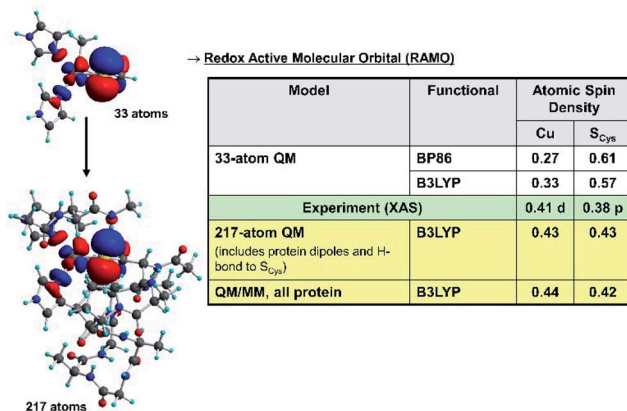


Fig. 11 GS wave function of the blue Cu active site by modern DFT. The RAMO contours for a small model (33 atoms) and a larger model (217 atoms) are shown on the left. The molecular orbital characters obtained using various functionals for both models, along with those obtained experimentally (from XAS in blue), are given in the table on the right. Reprinted with permission from ref. 3. Copyright (2006) American Chemical Society.

a second sphere mechanism for the protein to tune the redox potential of the active site over a range of ~ 200 mV for its ET function.²¹

We now focus on the experimental results in the middle row (blue) in Fig. 11 and the thiolate S π -orbital contribution in the RAMO contour of the blue Cu site (on the left), which were derived from new spectroscopic methods that we developed over the years to quantify covalency and define the nature of the metal-ligand bonding.

5. New spectroscopic methods in Bioinorganic Chemistry

Cu L-edge XAS enabled us to experimentally determine the amount of metal d character in the RAMO in Fig. 11. For Cu, the L-edge absorption is at ~ 930 eV and involves the Cu 2p transition to this RAMO (Fig. 12 right).²² The 2p is localized on the Cu and 2p \rightarrow 3d is electric dipole allowed, thus the intensity of this transition quantifies the amount of 3d character in the GS wave function of the blue Cu site [$\sqrt{(1 - \alpha^2)}$ in the right hand side of Fig. 12]. From the left hand side of Fig. 12, the L-edge absorption peak of the blue Cu site in plastocyanin (specifically the L₃-edge) is significantly lower in intensity than that of D_{4h} -[CuCl₄]²⁻, indicating that it has less d character and, thus, is more covalent. Since from the wide range of spectroscopies summarized in section 1, D_{4h} -[CuCl₄]²⁻ has $61 \pm 2\%$ $d_{x^2-y^2}$ character in its GS (Fig. 3C), the intensity ratio in the left hand side of Fig. 12 quantifies the blue Cu site as having 41% $d_{x^2-y^2}$ character, a very covalent active site, but with its covalency tuned by the second sphere effects of the protein, as shown in the bottom of Fig. 11.

The ligand responsible for this highly covalent blue Cu active site was defined by S K-edge XAS.¹⁵ We developed ligand K-edge XAS as a direct experimental method to quantify ligand character in GS wavefunctions.²³ The S K-edge is at ~ 2470 eV and, as shown in the right hand side of Fig. 13, it involves a transition

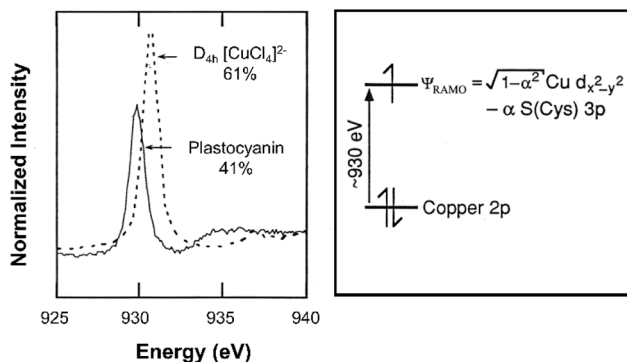


Fig. 12 Cu L-edge spectroscopy. L_3 -edge XAS spectrum of D_{4h} -[CuCl₄]²⁻ (dashed) and plastocyanin (solid) showing %Cu 3d character in RAMO on the left and the 2p → 3d transition on the right. Reprinted with permission from ref. 16. Copyright (2004) American Chemical Society.

from the S 1s orbital into the RAMO of the blue Cu center. Since the 1s orbital is localized on the sulfur and $s \rightarrow p$ is electric dipole allowed, the intensity of this S K-pre-edge transition directly reflects the Cys S_p character in the GS of the blue Cu site (α^2 in the right hand side of Fig. 13). From the left hand side of Fig. 13, the S K-pre-edge intensity of plastocyanin is 2.5 times as that of the tet b thiolate-Cu(II) model complex²⁴ that has 14% S_p character in its GS wave function. This quantified the blue Cu site in plastocyanin as having 38% Cys S_p character¹⁵ that will be proven in the next section to be key to its function in long range, rapid ET.

The third spectroscopic method that provided a key insight was the development of low temperature MCD to assign the unique absorption features of the blue Cu site (Fig. 6B) and from this determine the π - vs. σ -bonding interaction of the S_{Cys} with the Cu site.²⁵ From Fig. 14A (top two panels), at low temperature the absorption bands of the blue Cu absorption spectrum sharpen and, by correlating low temperature absorption with the low temperature CD (not shown) and low temperature MCD (Fig. 14A bottom), each method having a different selection

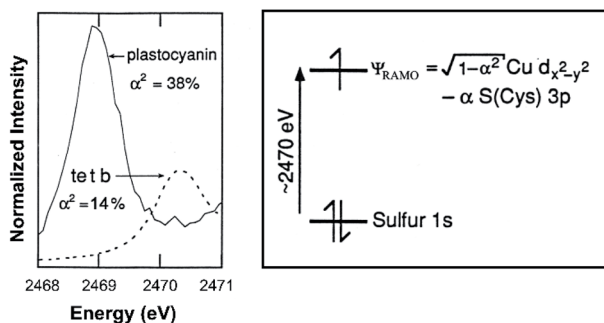


Fig. 13 Sulfur K-edge XAS. Left: K-edge XAS spectrum of the thiolate-Cu(II) model complex (dashed) and plastocyanin (solid), giving % S character in the GS. Right: 1s (S) → RAMO transition. Reprinted with permission from ref. 16. Copyright (2004) American Chemical Society.

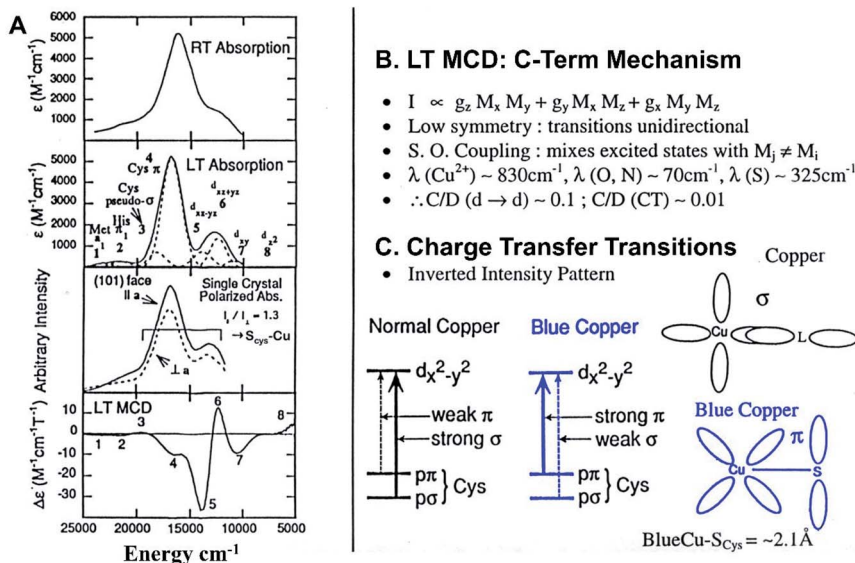


Fig. 14 Correlation of (A) room temperature, low temperature and single crystal polarized absorption and low temperature MCD spectra of plastocyanin, (B) low temperature MCD C-term mechanism and (C) charge transfer transitions in normal Cu (black) and blue Cu (blue) sites. Reprinted with permission from ref. 3. Copyright (2006) American Chemical Society.

rule, there are eight transitions required to fit the low temperature absorption spectrum of the blue Cu site in plastocyanin. Band 4 in the second panel of Fig. 14A is the characteristic intense absorption feature of the blue Cu site, while the lower energy band 6 has $\sim 20\%$ of this intensity. From polarized single crystal spectroscopy on plastocyanin (third panel of Fig. 14A), both bands have the same polarization ratio and, from correlation to the crystal structure (Fig. 7A), these are polarized along the Cu-S_{Cys} bond.

From section 2 and as illustrated in Fig. 14C, in “normal” Cu(II) complexes, the lobes of the $d_{x^2-y^2}$ orbital are oriented along the Cu-ligand bonds and the charge transfer spectrum exhibits a low energy weak π and higher energy intense σ transition. However, this is not the correct assignment of bands 6 and 4 of the blue Cu absorption spectrum, as revealed by the low temperature MCD spectrum at the bottom of Fig. 14A. Bands 5–8 are the most intense in the low temperature MCD spectrum relative to the absorption spectrum. As shown in Fig. 14B, MCD intensity requires two perpendicular transition moments (M_i), while in a low symmetry protein active site, all energy levels are non-degenerate. Thus, the electronic transitions are unidirectional. SOC is required to mix excited states with different polarizations to induce MCD intensity. Since the SOC parameter of Cu is large relative to that in the ligands, transitions that are intense in MCD relative to absorption (the C/D ratio) are assigned as $d \rightarrow d$ transitions. This is the case for bands 5–8. Alternatively, band 4, that is intense in absorption but weak in MCD, is the lowest energy, hence S_{Cys}- π CT, while a higher energy transition that is weak in absorption (band 3) is the S_{Cys}- σ to Cu $d_{x^2-y^2}$ CT. Thus, the blue Cu site has an inverted, lower energy intense π and higher energy weak σ CT and, since

CT intensity results from orbital overlap (right hand side of Fig. 14C), the $d_{x^2-y^2}$ orbital is rotated by 45° with its lobes bisected by the Cu–S_{Cys} bond. This orientation reflects the strong π -antibonding interaction of the thiolate with the Cu due to its short 2.1 Å Cu–S bond length.

Importantly the unique spectral features of the blue Cu site reflect a highly covalent thiolate S–Cu π -bond.

6. Electronic structure contributions to electron transfer

We now consider how this highly covalent thiolate S–Cu π -bond enables the function of the blue Cu site in long range, rapid ET. The focus is on H_{DA} , the electronic coupling between the electron donor and acceptor through protein pathways. A particularly interesting correlation is to the blue Cu site in multicopper oxidases, as the pathway for ET is well defined. As shown in Fig. 15A, the blue Cu site is near the surface of the enzyme, with its Cys ligand flanked on either side by His residues that are ligands of a buried trinuclear Cu cluster (TNC) site.²⁶ Electrons from the substrate are transferred to the blue Cu site and rapidly transferred over 13 Å through the Cis–His pathway to the TNC, where O₂ is reduced to water. As qualitatively visualized in Fig. 15A (green and yellow contours), the high covalency of the S_{Cys} in the GS wave function activates the Cis–His pathway for ET to the TNC. Quantitatively,¹⁸ as presented in Fig. 15B, H_{DA} increases linearly with the covalency of the Cu–S_{Cys} bond, with the rate of ET (k_{ET}) proportional to $(H_{DA})^2$ (see the Marcus equation for non-adiabatic ET, the bottom of Fig. 15A). From these calculations, there is one dominant superexchange pathway between the blue Cu center and Cu of the TNC, and this requires the π donation of the thiolate to the copper to activate a π electron–hole pathway through the protein backbone to go through a π to σ crossover to the catalytic site (Fig. 16C inset). Thus, the unique spectroscopic features of the blue Cu site reflect an electronic structure that is maximized for its ET function. We now consider the role of the protein in determining this electronic structure.

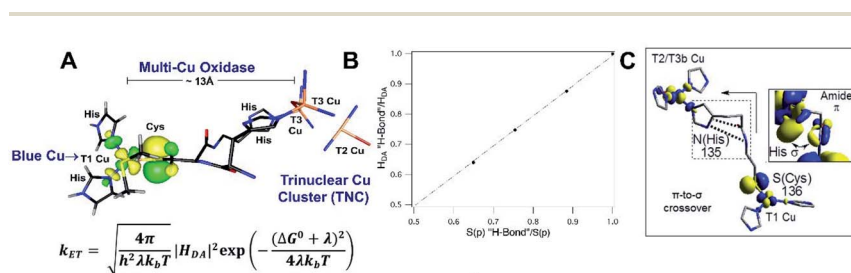


Fig. 15 (A) Active site of multicopper oxidases, showing blue Cu and TNC separated by ~ 13 Å and connected by a Cis–His pathway. The RAMO of the blue Cu site is shown in yellow and green contours. Given below is the Marcus equation for non-adiabatic ET; reprinted with permission from ref. 3. Copyright (2006) American Chemical Society. (B) Linear correlation between Cu–S covalency and H_{DA} and (C) molecular orbital involved in the Cis–His superexchange pathway from the blue Cu site to TNC. The inset shows the π to σ crossover. Reprinted with permission from ref. 18. Copyright (2014) American Chemical Society.

7. Role of the protein in determining the geometric and electronic structure of the blue copper site: the entatic state

Fig. 16A shows the absorption spectra of a series of blue Cu related proteins with the same Cys, Met and two His ligand set that vary from the blue color of plastocyanin to green in nitrite reductase (NiR). From Fig. 16A this color change reflects the fact that the CT transitions go from the inverted low energy intense π , high energy weak σ pattern of the blue Cu site to the “normal” low energy weak π and higher energy intense σ CT of the green site.²⁷

The structural changes associated with these spectral changes are given in Fig. 16B and C. In going from the blue Cu site to the green site, the thioether S_{Met} comes in from 2.9 to 2.5 Å, the thiolate goes out by 0.1 Å and the S-Cu-S plane rotates into the N-Cu-N plane, reflecting a Jahn-Teller distortion to a more tetragonal structure.

Thus, the protein is tuning the geometric and electronic structure of the Cu site and, from the correlation in Fig. 16B and C, this appeared to be controlled by the thioether Cu-S bond. This was tested by mutating the strong thioether Cu-S bond of the green site to a non-coordinating threonine.²⁸ As shown in Fig. 17A, this variant (M182T) expressed as a blue Cu site. Thus, the thioether ligation to the Cu is controlled by the protein. Its contribution to the function of the blue Cu site was revealed by additional studies on the green copper site in wild type NiR.²⁹ From Fig. 17B, this green site is in a thermodynamic equilibrium with a blue Cu site. The green Cu site is dominant at low temperatures, indicating that it is enthalpically favored and, from resonance Raman (rR), it has the strong Cu- S_{Met} bond (Fig. 16B).

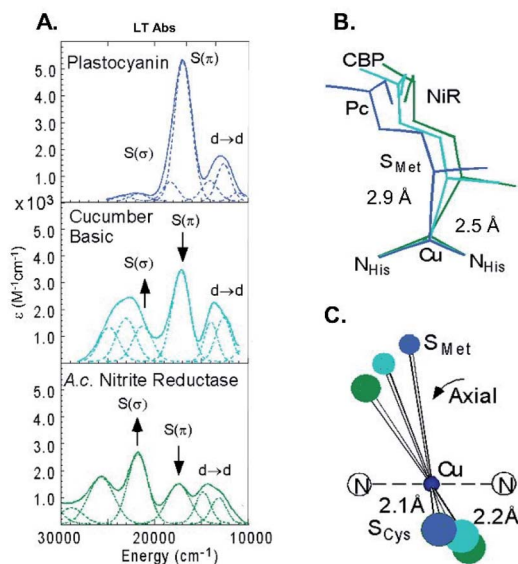


Fig. 16 (A) Absorption spectra of a series of active sites of related blue Cu proteins and (B) and (C) associated structural changes. Reprinted with permission from ref. 27. Copyright (1998) American Chemical Society.

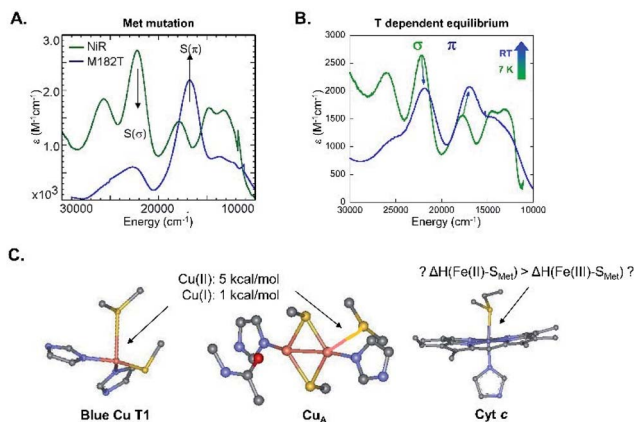


Fig. 17 (A) Absorption spectra of wild type NiR (green) and its M182T variant (blue); reprinted with permission from ref. 28. Copyright (2003) American Chemical Society. (B) Temperature dependent equilibrium between green and blue Cu sites; reprinted with permission from ref. 29. (C) Estimates of the Cu–S_{Met} bond enthalpies in blue Cu and Cu_A sites; presumed Fe–S_{Met} enthalpies in cyt *c*.

Increasing temperature results in its conversion to a blue Cu site which is, therefore, entropically favored and, from rR, there is no longer a Cu–S_{Met} bond. From a Van't Hoff analysis of this blue/green equilibrium, the enthalpic strength of the thioether Cu(II)–S bond is 5 kcal mol⁻¹. This is reproduced by DFT calculations which further give the strength of the thioether Cu(I)–S bond of the reduced site to be 1 kcal mol⁻¹ (Fig. 17C left). This study thus defined the entatic state of the blue Cu active site in proteins like plastocyanin (Fig. 6A). The thioether–Cu bond is weak, and the protein opposes the entropic contribution to the Gibbs free energy in keeping the thioether bound at physiological temperature. From the left hand side of Fig. 17C, this stabilizes the oxidized more than the reduced state of blue Cu sites and provides a first coordination sphere mechanism of lowering the reduction potential by ~200 mV. Parallel studies on the binuclear Cu_A site showed the same function of the thioether S–Cu bond, stabilizing the oxidized over the reduced state and lowering the potential (middle of Fig. 17C).³⁰

Alternatively, in cyt *c* (right hand side of Fig. 17C), it had been generally thought that the thioether Fe–S bond stabilized the reduced state more than the oxidized state and, thus, in contrast to the Cu protein ET active sites, the thioether Fe–S bond would raise the potential of cyt *c* by several hundred mV (relative to the partially unfolded protein).^{31–34} This potential difference in thioether Fe–S vs. Cu–S bonding led us to the experimental evaluation of the covalency of this Fe–S_{Met} bond in ferric and ferrous cyt *c*.³⁵

8. The Fe–S_{Met} bond in cyt *c*: contributions to function

A direct spectroscopic method to determine the covalency of the Fe–S_{Met} bond is L-edge XAS. From Fig. 18C for iron, this can probe both the dπ- and dσ-orbitals

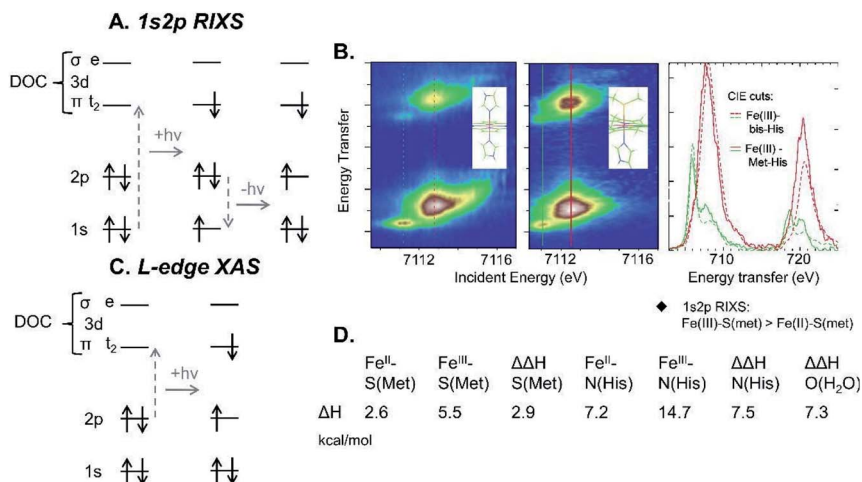


Fig. 18 (A) The photon absorption in the $1s \rightarrow 3d$ transition and photon energy emission in the subsequent $2p \rightarrow 1s$ transition in 1s2p RIXS. (B) 1s2p RIXS planes for a low spin bis-imidazole ferric compound (left), low spin ferric cyt *c* (middle) and constant incident energy cuts (L-edge like spectra) from RIXS planes (indicated by vertical lines in the RIXS spectra; green = π and red = σ contribution). (C) The $2p \rightarrow 3d$ transition in L-edge XAS. (D) Table showing DFT calculated Fe-S_{Met}, Fe-N_{His} and Fe-OH₂ enthalpic bond strengths for ferrous and ferric cyt *c*. Reprinted with permission from ref. 35. Copyright (2014) American Chemical Society.

and, thus, the differential orbital covalency (DOC) of cyt *c*.³⁶ However, there are issues with directly experimentally measuring L-edges on frozen protein solutions, so the K-edge was used to obtain the L-edge data through resonant inelastic X-ray scattering (1s2p RIXS). As shown in Fig. 18A, this involves measuring both the $1s \rightarrow 3d$ photon absorption (along the *x*-axis in Fig. 18B) and the photon emitted by the $2p$ electron filling the $1s$ core hole (*y*-axis in Fig. 18B). From the right side of Fig. 18A, this RIXS process results in the same final states as in L-edge XAS (Fig. 18C) but involves different selection rules.³⁷

The 1s2p RIXS spectrum of ferric cyt *c* is shown in the middle of Fig. 18B and vertical cuts through specific K-pre-edge features (on the *x*-axis) produced the L-edge like spectra, enhancing the π (green in the right hand side of Fig. 18B) and σ (red in the right hand side of Fig. 18B) contributions to the L-edge.³⁵ By modelling the L-edge like RIXS spectra of cyt *c*, it was experimentally determined that the Fe(III)-S_{Met} bond is in fact more covalent than the Fe(II)-S_{Met} bond, as determined above for Cu(II) vs. Cu(I) bonds. This was reproduced using DFT calculations, which further gave the enthalpic strength of the Fe(III)-S_{Met} bond as 2.9 kcal mol⁻¹ higher than that of Fe(II)-S_{Met} bond (Fig. 18D).

1s2p RIXS data were also obtained for a porphyrin model complex where the axial Met is replaced with an imidazole ligand (left hand side of Fig. 18B). Parallel studies on this complex show that the Fe(III)-N_{His} bond is, in fact, even stronger than that of Fe(II)-N_{His} bond with a $\Delta\Delta H$ of 7.5 kcal mol⁻¹ (Fig. 18D), which from calculations is also the case for an axial water ligand (Fig. 18D right). Thus, the Fe-S_{Met} bond does indeed increase the reduction potential, but this is relative to the His or water ligand that replaces it in a partially unfolded protein solution. The

results in Fig. 18D further showing that, as with the Cu active sites, the Fe-S_{Met} bond in cyt *c* is also very weak, in an entatic state imposed by the protein. For ferrous cyt *c*, this unconstrained Fe(II)-S_{Met} bond strength is only 2.6 kcal mol⁻¹.

The entatic nature of the cyt *c* active site was evaluated and quantified by ultrafast X-ray free electron laser (XFEL) experiments at the Linac Coherent Light Source (LCLS) at the SLAC National Accelerator Laboratory.³⁸ The experimental design is given in Fig. 19A. A 100 μ jet of ferrous cyt *c* is excited by a 50 fs 520 nm optical laser pulse. This excites the β-band of the porphyrin and heats the heme by ~100 °C. It takes ~6 ps for this heat to dissipate through the protein, thus the X-ray laser pulse was used to excite the Fe from 100 fs to ~20 ps. Two types of spectroscopies were utilized. The Kβ X-ray emission (XES) spectra in Fig. 19B are sensitive to the spin state of the Fe. The GS of ferrous cyt *c* in blue is a singlet, while the hot heme at 600 fs in red exhibits a lower energy multiplet feature at 7045 eV, showing that the heme is now in a quintet state. The K-edge XAS near edge spectra shown in Fig. 19C are sensitive to the local structure of the Fe. In going from the GS of ferrous cyt *c* in blue to the hot heme at 600 fs in red, there are shifts in the near edge features. These are shape resonances modelled using multiple scattering to determine that the thioether S is no longer bound to Fe when the heme is in the *S* = 2 state. Thus, the Kβ XES data could be used to monitor the binding of the thioether S to the Fe(II) as the heat dissipated from the heme (inset in Fig. 19D). This enabled an estimate of the strength of the thioether

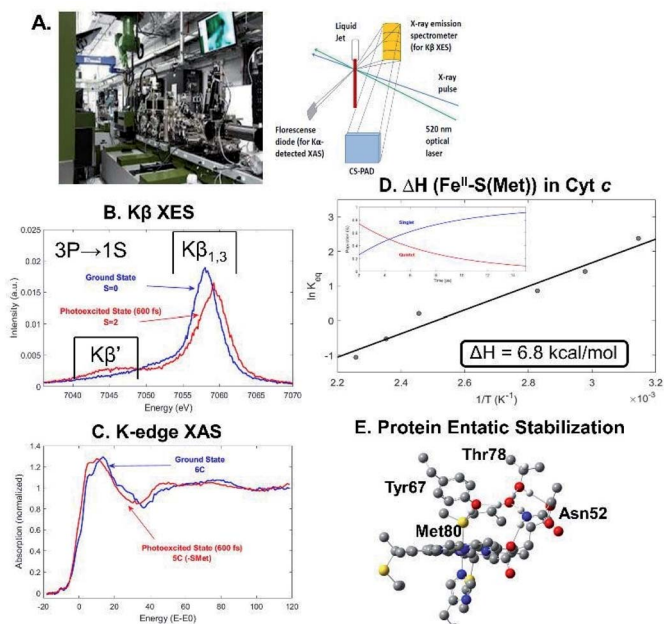


Fig. 19 (A) Ultrafast XFEL experimental setup and design at LCLS. (B) Kβ XES and (C) K-edge XAS spectra of the GS of ferrous cyt *c* (blue) and corresponding hot heme at 600 fs (red). (D) Plot used to estimate the strength of the Fe(II)-S_{Met} bond. In inset: populations of singlet (blue) and quintet (red) species obtained from XES modelling. (E) Active site of cyt *c*, showing an H-bond network to the Met in the protein pocket which stabilizes its Fe-S bond. From ref. 38. Reprinted with permission from AAAS.

Fe(II)–S bond in the protein as $6.8 \text{ kcal mol}^{-1}$. Relative to the ΔH of the free thioether Fe(II)–S bond in cyt *c* (Fig. 18D), this shows that the protein entatic state contribution stabilized this bond by $\sim 4 \text{ kcal mol}^{-1}$. As shown in Fig. 19E, this stabilization derives from an H-bond network to the Met in the protein pocket. This 4 kcal mol^{-1} is in a “sweet spot”, enabling the two physiological functions of cyt *c*. The presence of this bond enables its normal function of rapid ET to cytochrome *c* oxidase at the appropriate reduction potential to enable proton pumping for ATP synthesis. However, the Fe–S_{Met} bond is weak enough that in the membrane, this bond is ruptured by cardiolipin binding to cyt *c*, turning on its peroxidase function that permeabilizes the membrane, triggering apoptotic cell death.

9. Summary

This presentation emphasized three general themes of Bioinorganic Spectroscopy:

1. The wide range of spectroscopic methods in Fig. 2 provide complementary insights into the geometric and electronic structures of active sites, enabling structure–function correlations.
2. The correlation of spectroscopic results to electronic structure calculations provides deep insight into frontier molecular orbitals and reaction coordinates in catalysis.
3. The unique spectroscopic features that have dominated many areas of Bioinorganic Chemistry reflect novel geometric and electronic structures imposed on the active site by protein constraints that activate the metal center for its specific, efficient biological function.

Conflicts of interest

There are no conflicts to declare.

Acknowledgements

This work was supported by the National Institutes of Health grant R01DK031450 to E. I. S., who thanks his past students and collaborators for their contributions to this research.

References

- 1 R. H. Holm, P. Kennepohl and E. I. Solomon, *Chem. Rev.*, 1996, **96**, 2239–2314.
- 2 E. I. Solomon and M. A. Hanson, in *Inorganic Electronic Structure and Spectroscopy Vol. II*, eds. E. I. Solomon and A. P. B. Lever, John Wiley & Sons, Inc., New York, 1999, p. 1.
- 3 E. I. Solomon, *Inorg. Chem.*, 2006, **45**, 8012–8025.
- 4 E. I. Solomon, in *Comments on Inorganic Chemistry*, ed. N. Sutin, Gordon and Breach, New York, 1984, p. 225.
- 5 A. A. Gewirth, S. L. Cohen, H. J. Schugar and E. I. Solomon, *Inorg. Chem.*, 1987, **26**, 1133–1146.
- 6 P. Cassidy and M. A. Hitchman, *Inorg. Chem.*, 1977, **16**, 1568–1570.

- 7 R. S. Mulliken, C. A. Rieke, D. Orloff and H. Orloff, *J. Chem. Phys.*, 1949, **17**, 1248–1267.
- 8 S. R. Desjardins, K. W. Penfield, S. L. Cohen, R. L. Musselman and E. I. Solomon, *J. Am. Chem. Soc.*, 1983, **105**, 4590–4603.
- 9 R. A. Marcus and N. Sutin, *Biochim. Biophys. Acta, Rev. Bioenerg.*, 1985, **811**, 265–322.
- 10 P. M. Colman, H. C. Freeman, J. M. Guss, M. M. urata, V. A. Norris, J. A. M. Ramshaw and M. P. Venkatappa, *Nature*, 1978, **272**, 319–324.
- 11 B. L. Vallee and R. J. Williams, *Proc. Natl. Acad. Sci. U. S. A.*, 1968, **59**, 498–505.
- 12 H. B. Gray, B. G. Malmström and R. J. P. Williams, *J. Biol. Inorg. Chem.*, 2000, **5**, 551–559.
- 13 K. W. Penfield, R. R. Gay, R. S. Himmelwright, N. C. Eickman, V. A. Norris, H. C. Freeman and E. I. Solomon, *J. Am. Chem. Soc.*, 1981, **103**, 4382–4388.
- 14 J. E. Roberts, T. G. Brown, B. M. Hoffman and J. Peisach, *J. Am. Chem. Soc.*, 1980, **102**, 825–829.
- 15 S. E. Shadle, K. O. Hodgson, E. I. Solomon, B. Hedman and H. J. Schugar, *J. Am. Chem. Soc.*, 1993, **115**, 767–776.
- 16 E. I. Solomon, R. K. Szilagy, S. DeBeer George and L. Basumallick, *Chem. Rev.*, 2004, **104**, 419–458.
- 17 K. W. Penfield, A. A. Gewirth and E. I. Solomon, *J. Am. Chem. Soc.*, 1985, **107**, 4519–4529.
- 18 R. G. Hadt, S. I. Gorelsky and E. I. Solomon, *J. Am. Chem. Soc.*, 2014, **136**, 15034–15045, DOI: 10.1021/ja508361h.
- 19 S. Moon, S. Patchkovskii and D. R. Salahub, *J. Mol. Struct.*, 2003, **632**, 287–295.
- 20 S. Sinnecker and F. Neese, *J. Comput. Chem.*, 2006, **27**, 1463–1475.
- 21 R. G. Hadt, N. Sun, N. M. Marshall, K. O. Hodgson, B. Hedman, Y. Lu and E. I. Solomon, *J. Am. Chem. Soc.*, 2012, **134**, 16701–16716.
- 22 S. J. George, M. D. Lowery, E. I. Solomon and S. P. Cramer, *J. Am. Chem. Soc.*, 1993, **115**, 2968–2969.
- 23 B. Hedman, K. O. Hodgson and E. I. Solomon, *J. Am. Chem. Soc.*, 1990, **112**, 1643–1645.
- 24 J. L. Hughey, T. G. Fawcett, S. M. Rudich, R. A. Lalancette, J. A. Potenza and H. J. Schugar, *J. Am. Chem. Soc.*, 1979, **101**, 2617–2623.
- 25 A. A. Gewirth and E. I. Solomon, *J. Am. Chem. Soc.*, 1988, **110**, 3811–3819.
- 26 A. Messerschmidt and R. Huber, *Eur. J. Biochem.*, 1990, **187**, 341–352.
- 27 L. B. LaCroix, D. W. Randall, A. M. Nersissian, C. W. G. Hoitink, G. W. Canters, J. S. Valentine and E. I. Solomon, *J. Am. Chem. Soc.*, 1998, **120**, 9621–9631.
- 28 L. Basumallick, R. K. Szilagy, Y. Zhao, J. P. Shapleigh, C. P. Scholes and E. I. Solomon, *J. Am. Chem. Soc.*, 2003, **125**, 14784–14792.
- 29 S. Ghosh, X. Xie, A. Dey, Y. Sun, C. P. Scholes and E. I. Solomon, *Proc. Natl. Acad. Sci. U. S. A.*, 2009, **106**, 4969–4974.
- 30 M.-L. Tsai, R. G. Hadt, N. M. Marshall, T. D. Wilson, Y. Lu and E. I. Solomon, *Proc. Natl. Acad. Sci. U. S. A.*, 2013, **110**, 14658–14663.
- 31 A. L. Raphael and H. B. Gray, *Proteins: Struct., Funct., Bioinf.*, 1989, **6**, 338–340.
- 32 T. Ye, R. Kaur, F. T. Senguen, L. V Michel, K. L. Bren and S. J. Elliott, *J. Am. Chem. Soc.*, 2008, **130**, 6682–6683.
- 33 F. A. Tezcan, J. R. Winkler and H. B. Gray, *J. Am. Chem. Soc.*, 1998, **120**, 13383–13388.
- 34 H. Senn and K. Wuthrich, *Q. Rev. Biophys.*, 1985, **18**, 111–134.

- 35 T. Kroll, R. G. Hadt, S. A. Wilson, M. Lundberg, J. J. Yan, T.-C. Weng, D. Sokaras, R. Alonso-Mori, D. Casa, M. H. Upton, B. Hedman, K. O. Hodgson and E. I. Solomon, *J. Am. Chem. Soc.*, 2014, **136**, 18087–18099, DOI: 10.1021/ja5100367.
- 36 E. C. Wasinger, F. M. F. de Groot, B. Hedman, K. O. Hodgson and E. I. Solomon, *J. Am. Chem. Soc.*, 2003, **125**, 12894–12906.
- 37 M. Lundberg, T. Kroll, S. DeBeer, U. Bergmann, S. A. Wilson, P. Glatzel, D. Nordlund, B. Hedman, K. O. Hodgson and E. I. Solomon, *J. Am. Chem. Soc.*, 2013, **135**, 17121–17134.
- 38 M. W. Mara, R. G. Hadt, M. E. Reinhard, T. Kroll, H. Lim, R. W. Hartsock, R. Alonso-Mori, M. Chollet, J. M. Glowacki, S. Nelson, D. Sokaras, K. Kunnus, K. O. Hodgson, B. Hedman, U. Bergmann, K. J. Gaffney and E. I. Solomon, *Science*, 2017, **356**, 1276–1280.